Nano Research

Open Access

Research Article

High-voltage-resistant wafer-scale 4H-SiC ultraviolet photodetector with high uniformity enabled by electric field distribution modulation

Wanglong Wu[1], Shuo Liu[1], Zhiyuan Liu[2], Xinyun Zhou[1], Xiong Yang[3], Xinyun He[3], Qinglin Xia[1], Mianzeng Zhong[1] ✉, Jingbo Li[4] ✉, and Jun He[1] ✉

[1] *Hunan Key Laboratory of Nanophotonics and Devices, School of Physics, Central South University, Changsha 410083, China*
[2] *Guangdong Provincial Key Laboratory of Chip and Integration Technology, School of Semiconductor Science and Technology, South China Normal University, Foshan 528225, China*
[3] *Zhejiang Xinke Semiconductor Co., Ltd, Hangzhou 311421, China*
[4] *College of Optical Science and Engineering, Zhejiang University, Hangzhou 310027, China*

Cite this article: *Nano Research*, **2025**, *18*, 94907259. https://doi.org/10.26599/NR.2025.94907259

ABSTRACT: Wide bandgap semiconductors are ideal materials for ultraviolet (UV) photodetectors due to their stable optoelectronic properties and high efficient UV light absorption. However, photodetectors based on pure wide bandgap semiconductors typically have large dark current that inhibit the devices from generating high UV photoresponse. Herein, a high-voltage-resistant wafer-scale 4H-SiC UV photodetector enabled by electric field distribution modulation is proposed. As the P+ region introduced by the ion implantation process affects the electric field distribution and suppresses the Schottky barrier lowering effect, the dark current of the device reaches pA-level, and remains nA-level at a bias voltage of 1 kV. Meanwhile, the device exhibits superior photoresponse, including a prominent responsivity of 105.7 A/W, a remarkable detectivity of 1.01 × 10^{14} Jones, an outstanding photoconductive gain of 477, and a high light on/off ratio of 1.84 × 10^5. This device provides a reliable solution for high-performance UV photodetectors that require high-voltage-resistant in special areas, and the wafer-scale fabrication process makes it feasible for practical applications.

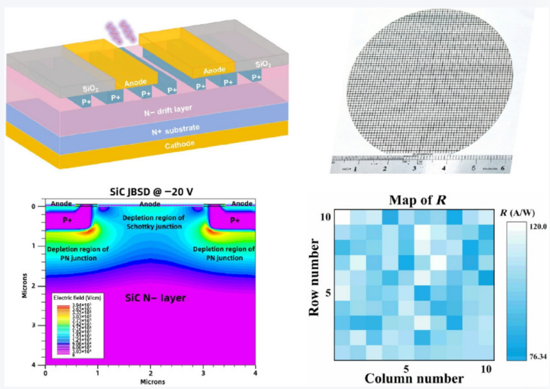

KEYWORDS: high-voltage-resistant, wafer-scale, 4H-SiC, electric field distribution, ultraviolet photodetector

1 Introduction

Ultraviolet (UV) photodetectors have important applications in diverse fields such as aerospace, medicine, military, optical communications, etc. [1–3]. The development of UV photodetectors can be divided into three stages, vacuum photomultiplier tubes, silicon-based photodiodes, and wide bandgap semiconductor-based detectors [4]. Among them, vacuum photomultiplier tubes are sensitive to high temperatures and radiation, while silicon-based photodiodes will respond to visible light and require additional filters [5]. Due to their large bandgap, wide bandgap semiconductors can effectively avoid responding to visible light, which eliminates the need for filters [6, 7]. In recent years, great efforts have been made to study UV photodetectors based on wide bandgap semiconductors and their heterostructures. For instance, Li et al. realized a high-performance GaN UV photodetector by nanoplasmonic enhancement [8]. Zhao et al. presented an ultrahigh responsivity self-powered solar-blind photodetector based on individual ZnO-Ga_2O_3 heterostructures [9]. Zhang et al. proposed a highly sensitive photodetector based on a photoinduced dynamic Schottky effect in 4H-SiC [10]. However, photodetectors exclusively based on wide bandgap semiconductors usually suffer from a larger dark current problem, which suppresses the photodetection performance of the device [4]. Therefore, researchers need to consider addressing this issue from the direction of nanostructure design and surface/interface modulation. Besides, compatibility of the devices with existing matured silicon-based semiconductor fabrication processes should also be

Received: November 28, 2024; **Revised:** January 13, 2025
Accepted: January 16, 2025

✉Address correspondence to Mianzeng Zhong, zmzhong@csu.edu.cn; Jingbo Li, jbli@zju.edu.cn; Jun He, junhe@csu.edu.cn

considered for better practical applications.

As a third generation semiconductor, 4H-structured silicon carbide (4H-SiC) is a high quality material for use as a visible blind UV detector, characterized by a wide bandgap (3.26 eV), high breakdown electric field, high electron saturation drift rate, and resistance to high temperature and radiation [10–12]. Besides, SiC is also compatible with silicon-based technologies as its thermal oxide is SiO_2 [13]. Typical pure 4H-SiC-based photodetectors are metal-semiconductor-metal photodiodes, Schottky barrier photodiodes (SBD) and p-i-n photodiodes, etc. The first two structure have Schottky contacts, and as the reverse bias voltage increases, both structures experience a decrease in the Schottky barrier, which leads to an increase in leakage current of the device and therefore an increase in the dark current of the photodetector [14, 15]. Herein, we have proposed a high-voltage-resistant wafer-scale 4H-SiC UV photodetector enabled by electric field distribution modulation to reduce the dark current of the device. By introducing a P+ region on the surface of conventional SBD through an ion implantation process, a junction barrier Schottky diode (JBSD) structure is formed. This structure could modulate the electric field distribution at the metal-semiconductor interface, thus suppressing the Schottky barrier lowering effect and reducing the dark current of the photodetector. Consequently, the dark current of the device reaches the pA-level and remains nA-level at 1 kV bias voltage. Meanwhile, the device exhibits remarkable UV photodetection performance, including a broad UV response from 240 to 380 nm, a responsivity of 105.7 A/W, a detectivity of 1.01×10^{14} Jones, a photoconductivity gain of 477, and a high light on/off ratio of 1.84×10^5. These excellent properties and the wafer-scale fabrication process make the device a reliable solution for high-performance UV photodetectors that require high-voltage-resistant in special areas.

2 Results and discussion

2.1 Wafer-scale fabrication and characterization of the JBSD photodetector

The wafer-scale fabrication process flow and structure of the device are shown in Fig. 1(a) and Fig. S1 in the Electronic Supplementary Material (ESM), respectively (see experimental section for details of device fabrication). In this device, the N− drift region and the P+ region were obtained by chemical vapor deposition and ion implantation, respectively. The electrode in contact with the N− drift region and the P+ region is the anode, while electrodes in contact with the substrate is cathode, and the conductive channel is vertical type. Besides, part of the N− and P+ regions are exposed as photosensitive areas. Mercury probe *C*–*V* test characterized the

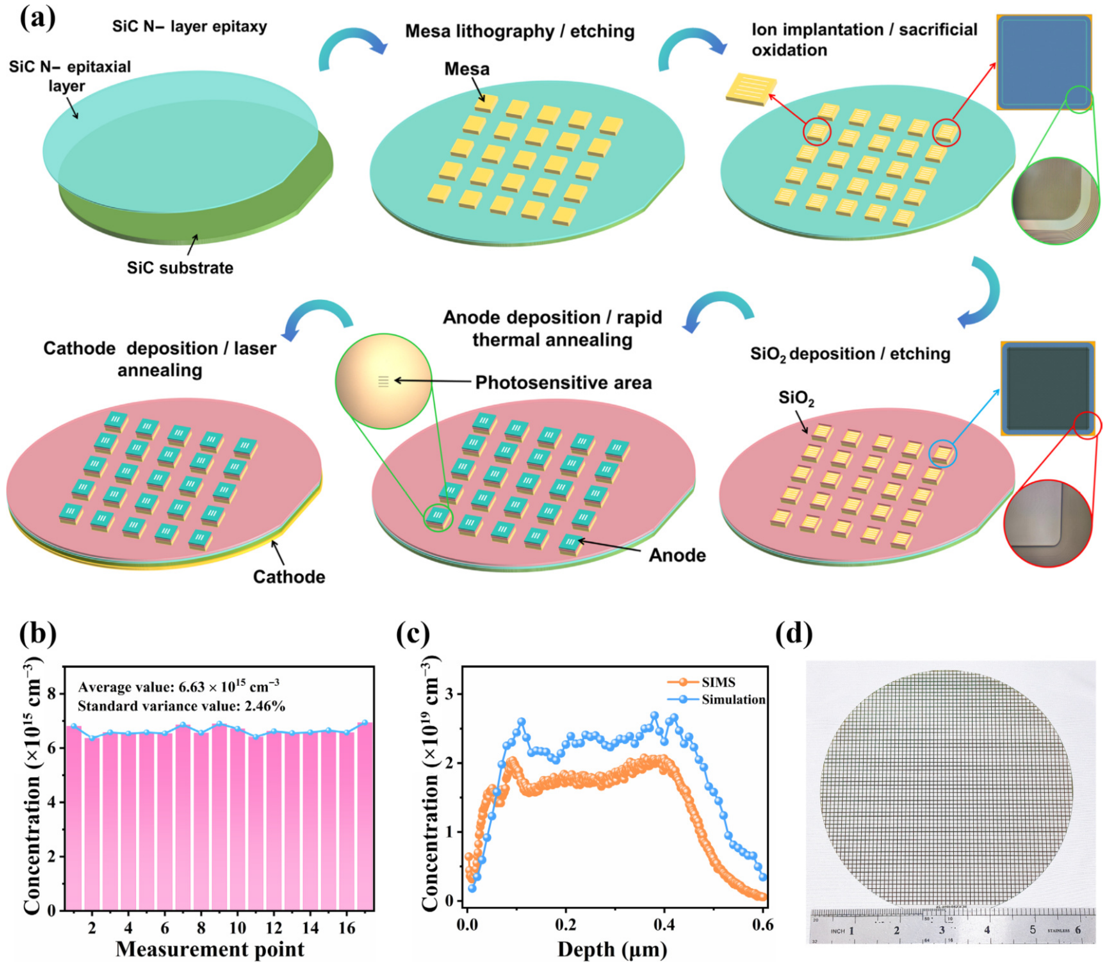

Figure 1 Wafer-scale fabrication process and characterization of the JBSD device. (a) Wafer-scale fabrication process flow diagram of the device. (b) Mercury probe *C*–*V* test results for carrier concentration in N− epitaxial layer. (c) TCAD software simulation and secondary ion mass spectrometer measurement of the depth and concentration of the ion-implanted P+ region. (d) Overall morphology of the wafer after fabrication.

carrier concentration of the N− epitaxial layer, as depicted in Fig. 1(b), 17 points were selected for the measurement, and the average carrier concentration obtained was 6.63 × 10^{15} cm^{-3} with a standard deviation of 2.46%, indicating that the concentration of the epitaxial layer was uniformly distributed. The concentration and depth characterization of the P+ region of the device are depicted in Fig. 1(c). Theoretical calculations and practical measurement results of the ion-implanted P+ region were carried out by Silvaco's TCAD software simulation and secondary ion mass spectrometry, respectively. The two results converge, while the actual value is slightly lower than the theoretical value, which is due to the fact that a thin SiO_2 mask layer (~ 50 nm) is reserved for ion implantation to reduce the channeling effect of ion implantation, which blocks some ions. Figure 1(d) shows the overall morphology of the JBSD device after fabrication on a 6-inch wafer.

2.2 Photoelectric properties of the JBSD photodetector

For convenience in testing, the anode and cathode of the device are connected to the source and drain, respectively (with the device in the off-state when V_{ds} > 0 V). Figure 2(a) presents the wavelength-dependent normalized current of the JBSD device at V_{ds} = 1 V. It can be seen that the device has a UV response from 240 to 380 nm with a peak response wavelength of approximately 301 nm. Thereafter, we studied the performance of the JBSD device under UV excitation at three different wavelengths, including 254, 275, and 365 nm. As shown in Fig. 2(b), the photoresponse under 275 nm is higher than the other two wavelengths. There may be two reasons for this phenomenon: Firstly, the cutoff wavelength of 4H-SiC is about 380 nm, while 4H-SiC is an indirect bandgap semiconductor, which results in low absorption coefficients near the cutoff wavelength, and lead to a weaker photoresponse [16]. Secondly, the depth of the P+ implantation region influences the peak response wavelength of the device [17], which leads to a larger response at 275 nm than 254 nm. The current–voltage (I–V) curves of the device in the dark and under 275 nm UV irradiation with different light power densities are then plotted in Fig. 2(c). Since the current of the device is large in the on-state and the photocurrent has less effect on it, we only study the optoelectronic performance of the device in the off-state. As illustrated in Fig. 2(d), with the increase of light power density, more photogenerated carriers are generated in the SiC and the photocurrent of the device increases. It is worth noting that the I–V curves of the device under illumination show a wave-like increase behavior, which is explained in Fig. S2 in the ESM. To evaluate the optoelectronic properties of the JBSD device comprehensively, we have calculated some basic figures-of-merit for the photodetection of the device, including photocurrent (I_{ph}),

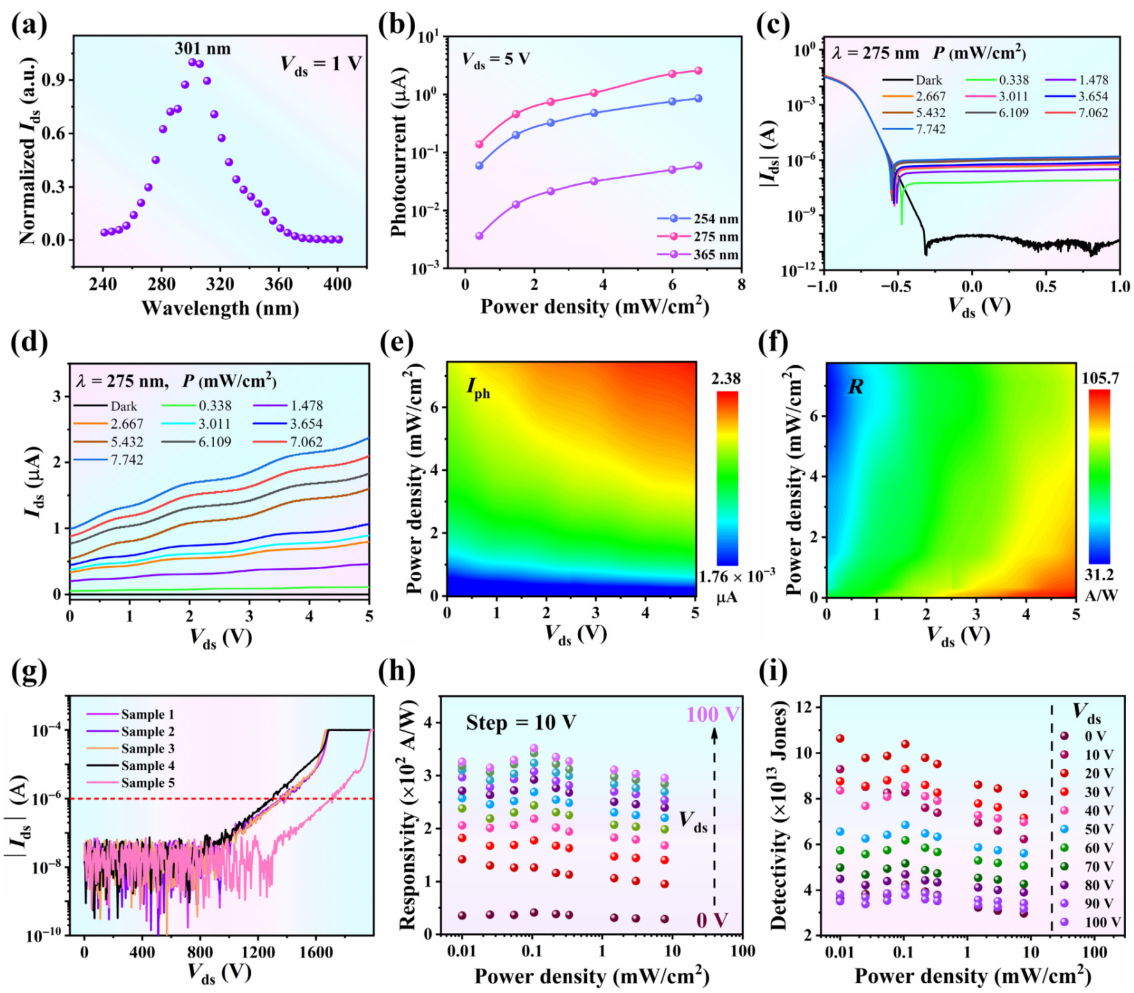

Figure 2 Photoresponse of the device, and optoelectronic performance at high bias voltages. (a) Wavelength-dependent normalized photocurrent of the JBSD device. (b) Comparison of I_{ph} of the device under 254, 275, and 365 nm UV illumination. (c) log and (d) linear I–V curves of the device at various light power densities under 275 nm illumination. 2D maps of (e) I_{ph} and (f) R as a function of V_{ds} and light power density. (g) Dark current variation of the device as V_{ds} increases. (h) R and (i) D^* of the device modulated by V_{ds} and light power density.

responsivity (R), detectivity (D^*), light on/off ratio (I_{on}/I_{off}), photoconductive gain (G), and rise/decay time (τ_{rise}/τ_{decay}), for details of the calculation method, please refer to Note S1 in the ESM. Figures 2(e) and 2(f) depict the dynamic variation of I_{ph} and R of the device with V_{ds} and light power density (under 275 nm illumination). Notably, I_{ph} and R can be effectively modulated by the bias voltage and power density. Additionally, we explored the performance of the device at high bias voltages. Figure 2(g) presents the dark current of the device as a function of bias voltage (five devices were selected for testing at different positions on the wafer). Remarkably, due to the presence of the P+ region, the dark current of the device is only 10 nA at V_{ds} = 1000 V. The I_{ds} of the device in Fig. 2(g) fluctuates widely when V_{ds} < 1000 V. This is due to the fact that when we are trying to measure the current of the device at high bias voltages (like greater than one kilovolt), we need to use the N1265A high-voltage expansion module of the Keysight B1505A source meter to conduct the measurement, but the current test accuracy of the expansion module is at the nA-level, hence the test value will oscillate rather significantly when the measured current is less than or equal to the nA-level. In Fig. 2(g), the breakdown voltage of sample 5 is greater than that of the other four samples, which is explained in Fig. S3 in the ESM. Figures 2(h) and 2(i) depict the variation of R and D^* of the JBSD device with light power density (under 275 nm illumination) and bias voltage, respectively. Significantly, the values of R and D^* vary within the same order of magnitude, and by increasing the V_{ds} to 100 V, the device still has a R of 352 A/W and a D^* of 4.23 × 10^{13} Jones, indicating that the device features high-voltage-resistant and high photodetection performance simultaneously. Besides, R presents a positive correlation with the bias voltage, while the peak value of D^* does not occur at the maximum bias voltage, which is owing to the fact that as bias voltage increases, the dark current of the device grows as well, which suppresses the enhancement of D^*.

The variation of I_{ph}, R, D^*, I_{on}/I_{off}, and G of the device with light power density under 275 nm illumination is illustrated in Figs. 3(a)–3(c). Among them, the dependence between I_{ph} and light power density could be fitted by $I_{ph} \propto P^{\alpha}$ [18–21]. The value of α reflects the generation mechanism of I_{ph} in the photodetector ($0 \leq \alpha \leq 1$), in which the closer α is to 1, the more the photoconductive effect dominates, whereas the closer α is to 0, the main mechanism of I_{ph} generation is the photogating effect [22–24]. The value of α obtained for this device is 0.988, indicating a photoconductive effect predominantly, and also suggesting that there are fewer defect recombination centers at the heterojunction interface [25, 26]. This is attributed to the sacrificial oxidation process performed after ion implantation to remove the damage and defects on the wafer surface to produce a high quality surface layer. With the increase of the light power density, the I_{on}/I_{off} of the device becomes progressively larger and could reach 1.84 × 10^5 at 7.742 mW/cm^2, exhibiting a robust logic swing characteristic (Fig. 3(b)). As can be seen from Figs. 3(a)–3(c), the maximum R, D^*, and G values of 105.7 A/W, 1.01 × 10^{14} Jones, and 477 were obtained for the device at a light power density of 0.036 mW/cm^2 for V_{ds} = 5 V, respectively. Meanwhile, the values of R, D^*, and G decrease with the increase of light power density, which can be ascribed to the enhancement of the Auger recombination rate of photogenerated carriers at higher light power densities [27, 28]. The optoelectronic performance of the device at higher bias voltage (V_{ds} = 20 V) or under 254/365 nm illumination is shown in Figs. S4–S6 in the ESM, respectively. Figure 3(d) portrays the dynamic photoresponse of the device under various light power densities, where the device is observed to possess a robust photocurrent switching behavior.

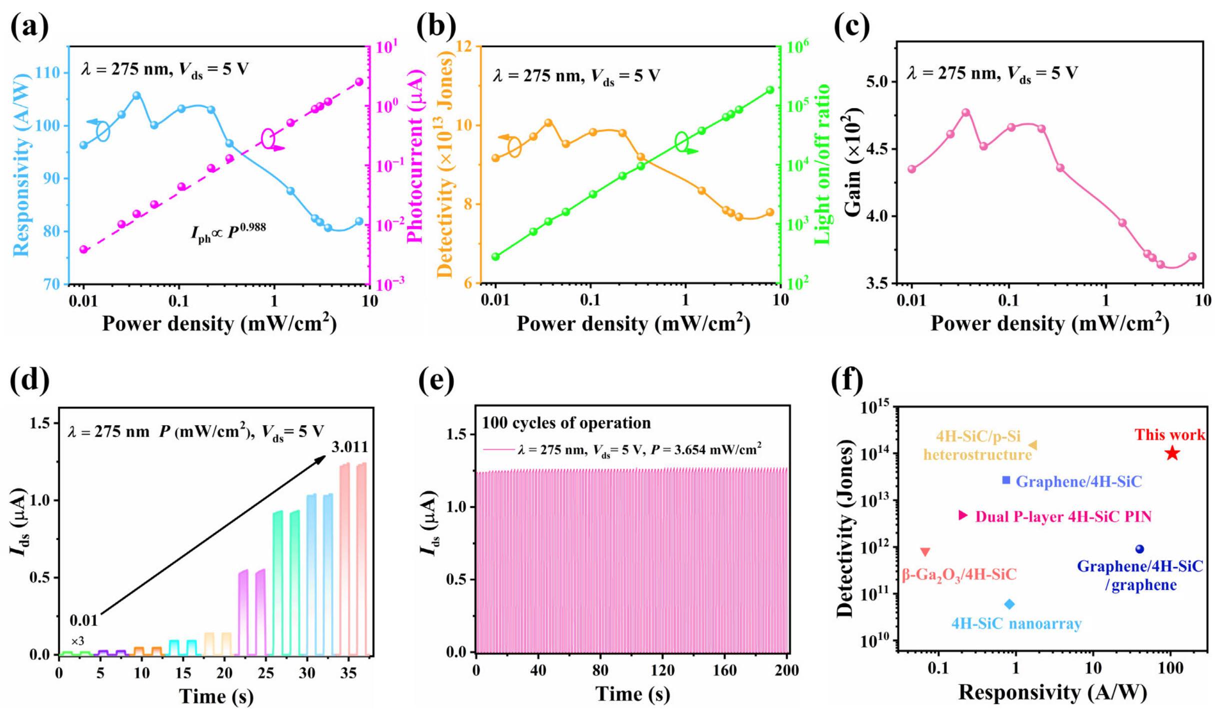

Figure 3 Optoelectronic performance of the JBSD device under 275 nm illumination. (a)–(c) Variation of responsivity, photocurrent, detectivity, light on/off ratio and photoconductive gain with light power density. (d) Dynamic photoresponse of the device at different light power densities. (e) Optoelectronic switching behavior of the device over long periods of time (100 cycles of operation). (f) Comparison of responsivity and detectivity of the JBSD device with previously reported 4H-SiC-based photodetectors, including 4H-SiC/p-Si heterostructure [29], graphene/4H-SiC [30], dual P-layer 4H-SiC PIN [31], β-Ga_2O_3/4H-SiC [32], graphene/4H-SiC/graphene [33], and 4H-SiC nanoarray [34].

Moreover, Fig. 3(e) shows that after 100 cycles of operation, the photocurrent of the device still tends to stabilize without significant fluctuation, confirming the excellent cyclability and stability of the JBSD photodetector. The transient photoresponse of the device is presented in Fig. S7 in the ESM, the τ_{rise} and τ_{decay} were calculated to be about 2.67 and 3.01 ms, respectively. Figures S8 and S9 in the ESM demonstrate the performance of the device after a month of placement and retesting, which is essentially the same as the previous results, emphasizing the high stability of the JBSD device over time. Additionally, the performance of our 4H-SiC JBSD device is compared with those previously reported 4H-SiC-based photodetectors in Fig. 3(f). It could be appreciated that our device exhibits prominent performances, implying that it is advanced in the category of similar photodetectors.

2.3 Operation mechanism and application of the JBSD photodetector

Considering the related Refs. [30, 35, 36], we present the energy band diagram of the JBSD device under illumination in Figs. 4(a) and 4(b). Since the work function of both the metal Ti and P-SiC is higher than N-SiC, the energy band bends and forms a built-in electric field ($E_{built-in}$) pointing from N-SiC to Ti and N-SiC to P-SiC, respectively. Under illumination, electrons in the valence band of both the exposed N-SiC and P-SiC regions are excited to their conduction band, hence generating photogenerated electron-hole pairs. Driven by the $E_{built-in}$, photogenerated electrons at the N-SiC interface move deeper into the epitaxial layer, and photogenerated electrons in P-SiC move towards N-SiC. The presence of these two $E_{built-in}$ facilitates the spatial separation of the photocarriers in SiC, and the photogenerated electrons participate in the external circuit circulation under the applied V_{ds}, which generates the photocurrent. The spatial separation of the photocarriers could suppress their recombination potentially, providing a high photoconductivity gain [37, 38].

To investigate the effect of the ion-implanted P+ region on the performance of the device, we performed finite element simulations of the electric field distribution of the device. As shown in Fig. 4(c), the peak electric field of the device occurs at the metal-semiconductor interface when the bias voltage is zero. And when reverse bias voltage is applied and the device is in the off-state, the PN junction is also in the reverse biased state. As the reverse bias voltage increases, the depletion region formed by the PN junction continuously extends towards the Schottky region and eventually combines with the depletion region below the Schottky barrier, as depicted in Figs. 4(d) and 4(e). Once the depletion region combines, the conducting channel is pinched off and an electron barrier is formed below the channel, and as the reverse bias voltage increases, the depletion region extends below the channel and the increased reverse voltage will be sustained by the depletion region. The electron barrier shields the Schottky barrier from high electric fields, effectively suppressing the Schottky barrier lowering effect [15, 39], resulting in a significant reduction in the dark current of the JBSD photodetector compared to the SBD photodetector. The simulation of the electric field distribution of the SBD device under the same conditions is illustrated in Fig. S10 in the ESM. Due to the absence of the P+ region, the peak electric field at the metal-semiconductor interface keeps increasing with the increase of reverse bias voltage, which also leads to a decrease in the Schottky barrier, causing more electrons to tunnel and increasing the dark current of the SBD photodetector [15, 40]. It suggests that the JBSD structure can effectively modulate the electric field distribution to enable the device with lower dark current at higher bias voltage. A comparison of the dark current and photocurrent of the JBSD device and the SBD device is shown in Fig. S11 in the ESM, and the optoelectronic performance of the SBD device is shown in Fig. S12 in the ESM.

To verify the uniformity of the device on the wafer, 100 devices were selected for testing (under identical conditions) and the corresponding R, D^*, and G values were calculated. As presented in Figs. 5(a)–5(c), the devices all exhibit excellent optoelectronic

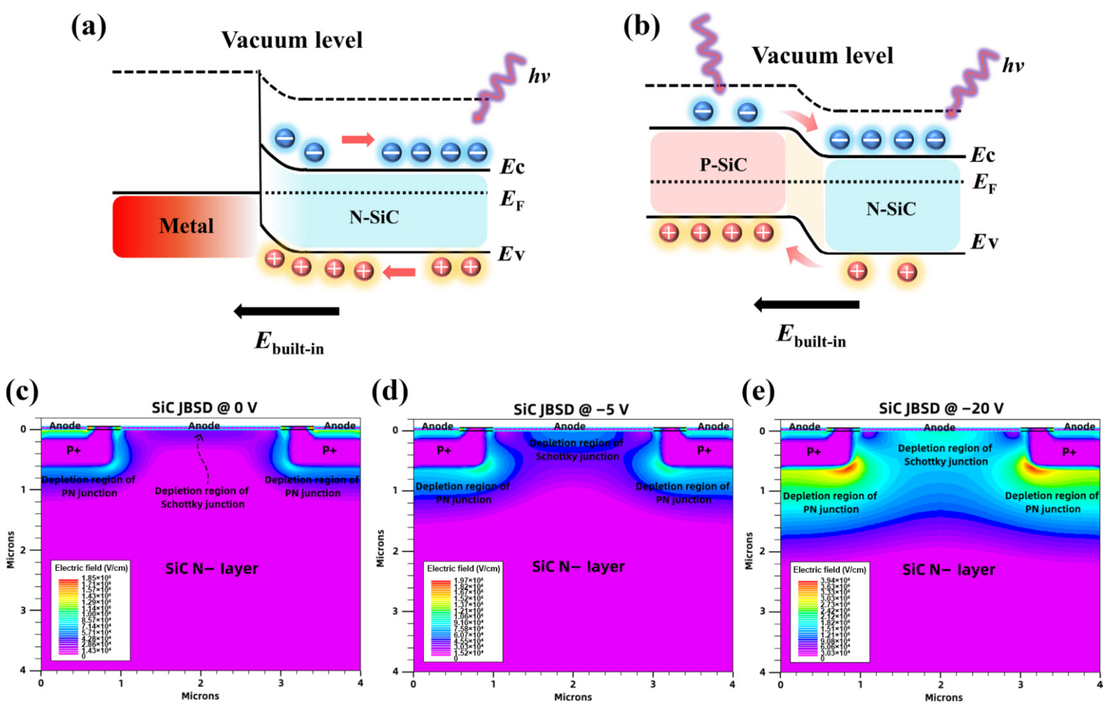

Figure 4 Photoresponse mechanism of the JBSD device. Energy band diagram of (a) metal (Ti) and N-SiC, (b) P-SiC and N-SiC under UV illumination. (c)–(e) Simulation of electric field distribution of the JBSD device at 0, −5, and −20 V bias voltage (with the device in the off-state).

performance, and the difference basically varies within one order of magnitude, demonstrating that the JBSD photodetector using the wafer-scale fabrication process has a high uniformity. Furthermore, this also indicates that the JBSD device has potential array imaging capabilities. Therefore, we validated the imaging capability of individual device. As shown in Fig. 5(d), the 365 nm UV light is used as the light source, the mask is controlled by a motor which moves in a two-dimensional direction, the pattern on the mask is a "W" character, and the JBSD device is used as an individual sensing pixel. When UV light passes through the transparent part of the mask and illuminates the JBSD device, the photocurrent is generated by the device and was synchronously recorded by a source meter. The motor controls the movement of the mask in a two-dimensional direction to produce a position-dependent photocurrent mapping image. Figures 5(e)–5(g) present the mapping images of the output 'W' of the JBSD device at V_{ds} = 5 V, V_{ds} = 10 V, and V_{ds} = 15 V, respectively, all within the same current range. Notably, the device could recognize and output the "W" character at all three bias voltages, and has a high pixel and contrast ratio at V_{ds} = 15 V. Accordingly, the JBSD device has great potential for future UV array imaging applications.

3 Conclusions

In summary, we have successfully fabricated a high-voltage-resistant wafer-scale 4H-SiC UV photodetector enabled by electric field distribution modulation to reduce the dark current. As the P+ region introduced by the ion implantation process affects the electric field distribution and suppresses the Schottky barrier lowering effect, the dark current of the device reaches pA-level, and still has nA-level dark current at a bias voltage of 1 kV. Meanwhile, the device exhibits remarkable UV photodetection performance, including a broad UV response from 240 to 380 nm, a responsivity of 105.7 A/W, a detectivity of 1.01 × 10^{14} Jones, a photoconductivity gain of 477, and a high light on/off ratio of 1.84 × 10^{5}. Additionally, the optoelectronic performance of the device exhibits high uniformity under wafer-scale fabrication process, and features high-resolution imaging capability. These excellent properties and the wafer-scale fabrication process make the device a reliable solution for high-performance UV photodetectors that require high-voltage-resistant in special areas.

4 Experimental methods

4.1 Fabrication of the device

First of all, a 13 μm, 6.63 × 10^{15} cm^{-3} N− epitaxial layer was deposited on the surface of a 6-inch SiC substrate (Guangzhou Nansha Wafer Semiconductor Technology Co., Ltd., 350 μm, 3 × 10^{19} cm^{-3}) using chemical vapor deposition (AIXTRON, G5WWC). Secondly, the mesa was dry etched on the wafer surface by photolithography (Nikon Stepper NSR2005 i8) and inductively coupled plasma etching (ICP, Shanghai Winetch Semiconductor Technology Co., Ltd., Wincros-150). Subsequently, P+ doping with a depth of 400 nm and a concentration of 1.5 × 10^{19} cm^{-3} was formed by ion implantation (ULVAC, IH-860PSIC-II), and the doped ions were diffused at high temperature using an activation furnace (Jihua Hengyi Semiconductor Science and Technology Co., Ltd., HY-AF150). Then, a 30 nm oxide layer was formed on the surface of the wafer using a high temperature oxidation furnace (XinWei Electronics Equipment Co., Ltd., TEL-α8), and was removed by buffered oxide etch. Next, a 1 μm SiO_2 layer was

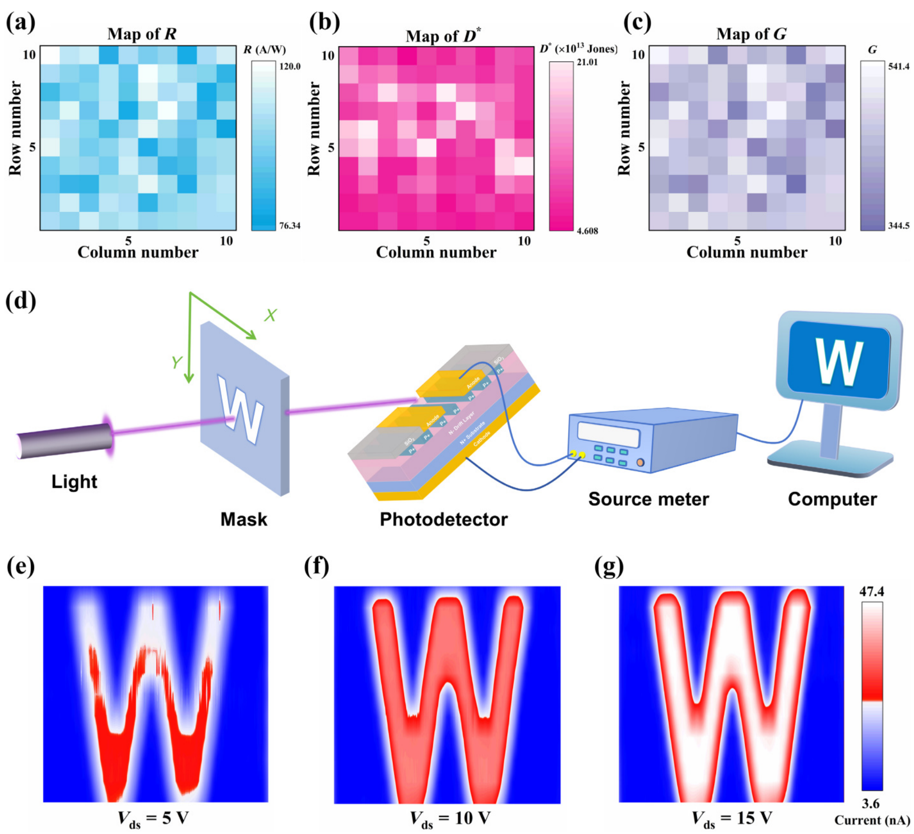

Figure 5 Wafer-scale test and imaging application of the JBSD device. (a)–(c) Map of *R*, *D**, and *G* for 100 devices on the wafer. (d) Schematic diagram of the device imaging. (e)–(g) The JBSD device outputs the corresponding image of "W" at V_{ds} = 5, 10, 15 V.

deposited by plasma enhanced chemical vapor deposition (PECVD, NAURA , EPEE 550). Afterward, Ti/Al metal of 100/200 nm was deposited as anode on the front side of the wafer using Electron Beam Evaporation (EBE, Taiwan FuLin Technology and Engineering Co., Ltd., FU-20PEB-ITO) , followed by a rapid thermal annealing at 450 °C for 5 min (Larcomse, LH-RTA-E) to form a Schottky contact. As the front side process is completed, a grinder (TSMID, TFG-3200) is used to thin the back side of the wafer to 170 μm to reduce the on-resistance of the device and the drift path of the carriers to increase the photoresponse of the device. After that, 100 nm Ni was sputtered on the backside of the wafer by magnetron sputtering (EVATEC, RADIANCE), with laser annealing (Jihua Hengyi Semiconductor Technology Co., Ltd., JT 180) to form an ohmic contact. Finally, Ti/Ni/Al/Ti/Ag metals of 100 nm/150 nm/1.5 μm/100 nm/300 nm were deposited as cathodes on the backside of the wafer by EBE.

4.2 Characterization and measurement

The mercury probe *C*–*V* test (MICROAHEAD, MCV-200) was used to characterize the carrier concentration of the N– epitaxial layer. The depth and concentration of the ion-implanted P+ region were measured by secondary ion mass spectrometry (CAMECA, IMS 7f-Auto). The wavelength-dependent photoresponse was tested by a spectrometer (Microenergyc, CME-TLSX300UV-3G). A 254/275/365 nm ultraviolet LED (UVGO) driven by a DC power supply (Zhaoxin, FPS 325D) was used as the light source, and the electrical and optical response of the device was tested by connecting a source meter ((KEITHLEY, 2612B) to the probe stage. The breakdown voltage of the device was tested by a power device analyzer (Keysight, B1505A). Finite element analysis of the electric field distribution of the device was carried out using Technology Computer Aided Design (TCAD, Silvaco) software.

Electronic Supplementary Material: Supplementary material (calculation of key figures-of-merit for the JBSD photodetector, structure of the JBSD device, explanation of the wave-like increase behavior in the *I*–*V* curve of the JBSD device under illumination, performance of the JBSD device under 275 nm illumination (V_{ds} = 20 V), performance of the JBSD device under 254/365 nm illumination, single-cycle photoresponse of the JBSD device under 275 nm illumination, optoelectric properties of the JBSD device after one month, simulation of electric field distribution of the SBD device, comparison of dark current and photocurrent of SBD and JBSD device and performance of the SBD device under 275 nm illumination) is available in the online version of this article at https://doi.org/10.26599/NR.2025.94907259.

Data availability

All data needed to support the conclusions in the paper are presented in the manuscript and the Electronic Supplementary Material. Additional data related to this paper may be requested from the corresponding author upon request.

Acknowledgements

This work was financially supported by the National Natural Science Foundation of China (Nos. 12174451, 12474080, and 12274467), the Science and Technology Innovation Program of Hunan Province (No. 2022RC1199), the High Performance Computing Center of Central South University, Central South University Graduate Student Independent Exploration and Innovation Project (Nos. 2024ZZTS0454 and 2024ZZTS0778).

Declaration of competing interest

All the contributing authors report no conflict of interests in this work.

Author contribution statement

W. L. W.: Data curation (lead); investigation (lead); writing – original draft (lead); writing – review & editing (equal); formal analysis (lead); conceptualization (equal); visualization (lead). S. L.: Data curation (equal); formal analysis (equal); visualization (equal). Z. Y. L.: Formal analysis (equal); visualization (equal). X. Y. Z.: Visualization (equal). X. Y.: Data curation (equal); formal analysis (equal). X. Y. H.: Data curation (equal). Q. L. X.: Funding acquisition (equal); resources (equal). M. Z. Z.: Funding acquisition (lead); resources (equal); supervision (lead); conceptualization (lead); writing – review & editing (lead). J. B. L.: Resources (lead); supervision (equal); conceptualization (equal). J. H.: Funding acquisition (equal); project administration (equal); supervision (equal). All the authors have approved the final manuscript.

Use of AI statement

None.

References

[1] Hatch, S. M.; Briscoe, J.; Dunn, S. A self-powered ZnO-nanorod/CuSCN UV photodetector exhibiting rapid response. *Adv. Mater.* **2013**, *25*, 867–871.
[2] Kong, W. Y.; Wu, G. A.; Wang, K. Y.; Zhang, T. F.; Zou, Y. F.; Wang, D. D.; Luo, L. B. Graphene-β–Ga_2O_3 heterojunction for highly sensitive deep UV photodetector application. *Adv. Mater.* **2016**, *28*, 10725–10731.
[3] Gong, C. H.; Chu, J. W.; Qian, S. F.; Yin, C. J.; Hu, X. Z.; Wang, H. B.; Wang, Y.; Ding, X.; Jiang, S. C.; Li, A. L. et al. Large-scale ultrathin 2D wide-bandgap BiOBr nanoflakes for gate-controlled deep-ultraviolet phototransistors. *Adv. Mater.* **2020**, *32*, 1908242.
[4] Cao, F.; Liu, Y.; Liu, M.; Han, Z. Y.; Xu, X. B.; Fan, Q. L.; Sun, B. Wide bandgap semiconductors for ultraviolet photodetectors: Approaches, applications, and prospects. *Research* **2024**, *7*, 0385.
[5] Wu, W. L.; Liu, C. K.; Han, L. X.; Wang, X. Z.; Li, J. B. Wafer-scale high sensitive UV photodetectors based on novel AlGaN/n-GaN/p-GaN heterostructure HEMT. *Appl. Surf. Sci.* **2023**, *618*, 156618.
[6] Um, D. Y.; Chandran, B.; Kim, J. Y.; Oh, J. K.; Kim, S. U.; An, J. U.; Lee, C. R.; Ra, Y. H. New charge carrier transport-assisting paths in ultra-long GaN microwire UV photodetector. *Adv. Funct. Mater.* **2023**, *33*, 2306143.
[7] Chen, M. X.; Zhao, B.; Hu, G. F.; Fang, X. S.; Wang, H.; Wang, L.; Luo, J.; Han, X.; Wang, X. D.; Pan, C. F. et al. Piezo-phototronic effect modulated deep UV photodetector based on ZnO-Ga_2O_3 heterojuction microwire. *Adv. Funct. Mater.* **2018**, *28*, 1706379.
[8] Li, D. B.; Sun, X. J.; Song, H.; Li, Z. M.; Chen, Y. R.; Jiang, H.; Miao, G. Q. Realization of a high-performance GaN UV detector by nanoplasmonic enhancement. *Adv. Mater.* **2012**, *24*, 845–849.
[9] Zhao, B.; Wang, F.; Chen, H. Y.; Zheng, L. X.; Su, L. X.; Zhao, D. X.; Fang, X. S. An ultrahigh responsivity (9.7 mA·W^{-1}) self-powered solar-blind photodetector based on individual ZnO-Ga_2O_3 heterostructures. *Adv. Funct. Mater.* **2017**, *27*, 1700264.
[10] Zhang, Y. M.; Wang, Y. C.; Wang, L. F.; Zhu, L. P.; Wang, Z. L. Highly sensitive photoelectric detection and imaging enhanced by the

pyro-phototronic effect based on a photoinduced dynamic schottky effect in 4H-SiC. *Adv. Mater.* **2022**, *34*, 2204363.
[11] Hicks, J.; Tejeda, A.; Taleb-Ibrahimi, A.; Nevius, M. S.; Wang, F.; Shepperd, K.; Palmer, J.; Bertran, F.; Le Fèvre, P.; Kunc, J. et al. A wide-bandgap metal-semiconductor-metal nanostructure made entirely from graphene. *Nat. Phys.* **2013**, *9*, 49–54.
[12] Siddiqui, A.; Khosa, R. Y.; Usman, M. High-k dielectrics for 4H-silicon carbide: Present status and future perspectives. *J. Mater. Chem. C* **2021**, *9*, 5055–5081.
[13] Yin, Z. P.; Yang, C.; Zhang, F. L.; Su, Y.; Qin, F. W.; Wang, D. J. Low-temperature re-oxidation of near-interface defects and voltage stability in SiC MOS capacitors. *Appl. Surf. Sci.* **2020**, *531*, 147312.
[14] Okino, H.; Kameshiro, N.; Konishi, K.; Shima, A.; Yamada, R. I. Analysis of high reverse currents of 4H-SiC Schottky-barrier diodes. *J. Appl. Phys.* **2017**, *122*, 235704.
[15] She, X.; Huang, A. Q.; Lucía, Ó.; Ozpineci, B. Review of silicon carbide power devices and their applications. *IEEE Trans. Ind. Electron.* **2017**, *64*, 8193–8205.
[16] Shen, Y.; Jones, A. H.; Yuan, Y.; Zheng, J. Y.; Peng, Y. W.; VanMil, B.; Olver, K.; Sampath, A. V.; Parker, C.; Opila, E. et al. Near ultraviolet enhanced 4H-SiC schottky diode. *Appl. Phys. Lett.* **2019**, *115*, 261101.
[17] Hou, Y. S.; Sun, C. Z.; Wu, J. K.; Hong, R. D.; Cai, J. F.; Chen, X. P.; Lin, D. Q.; Wu, Z. Y. Effect of epitaxial layer's thickness on spectral response of 4H-SiC P-I-N ultraviolet photodiodes. *Electron. Lett.* **2019**, *55*, 216–218.
[18] Zhang, F.; Mo, Z. X.; Cui, B. C.; Liu, S.; Xia, Q. L.; Li, B.; Li, L. W.; Zhang, Z. W.; He, J.; Zhong, M. Z. Bandgap engineering of BiIns nanowire for wide-spectrum, high-responsivity, and polarimetric-sensitive detection. *Adv. Funct. Mater.* **2023**, *33*, 2306077.
[19] Zhang, F.; Yu, Y. L.; Mo, Z. X.; Huang, L.; Xia, Q. L.; Li, B.; Zhong, M. Z.; He, J. Alloying-engineered high-performance broadband polarized $Bi_{1.3}In_{0.7}Se_3$ photodetector with ultrafast response. *Nano Res.* **2022**, *15*, 8451–8457.
[20] Mo, Z. X.; Zhang, F.; Wang, D. Y.; Cui, B. C.; Xia, Q. L.; Li, B.; He, J.; Zhong, M. Z. Ultrafast-response and broad-spectrum polarization sensitive photodetector based on $Bi_{1.85}In_{0.15}S_3$ nanowire. *Appl. Phys. Lett.* **2022**, *120*, 201105.
[21] Zhong, M. Z.; Cui, B. C.; Mo, Z. X.; Yu, Y. L.; Xia, Q. L.; Zhang, F.; Zhou, Z. Q.; Huang, L.; Li, B.; Yang, J. H. et al. Gate controllable band alignment transition in 2D black-arsenic/WSe_2 heterostructure. *Appl. Phys. Rev.* **2023**, *10*, 021416.
[22] Luo, P.; Zhuge, F. W.; Wang, F. K.; Lian, L. Y.; Liu, K. L.; Zhang, J. B.; Zhai, T. Y. PbSe quantum dots sensitized high-mobility Bi_2O_2Se nanosheets for high-performance and broadband photodetection beyond 2 μm. *ACS Nano* **2019**, *13*, 9028–9037.
[23] Wu, W. L.; Liu, Z. Y.; Qiu, Z. C.; Wu, Z. Q.; Li, Z. M.; Yang, X.; Han, L. X.; Li, C. Y.; Huo, N. J.; Wang, X. Z. et al. An ultrasensitive $ReSe_2$/WSe_2 heterojunction photodetector enabled by gate modulation and its development in polarization state identification. *Adv. Opt. Mater.* **2024**, *12*, 2301410.
[24] Zhao, F. P.; Wang, D. Y.; Zhang, F.; Cui, B. C.; Xia, Q. L.; Zhong, M. Z. Gate-controlled photoresponse improvement in b-AsP/WSe_2 heterostructures with type-I band alignment. *Appl. Phys. Lett.* **2023**, *122*, 151105.
[25] Aichinger, T.; Lenahan, P. M.; Tuttle, B. R.; Peters, D. A nitrogen-related deep level defect in ion implanted 4H-SiC pn junctions—A spin dependent recombination study. *Appl. Phys. Lett.* **2012**, *100*, 112113.
[26] Zhang, F.; Shi, H.; Yu, Y. L.; Liu, S.; Liu, D. Y.; Zhou, X. Y.; Yuan, L.; Shi, J. Q.; Xia, Q. L.; Wei, Z. M. et al. Dynamic band-alignment modulation in $MoTe_2$/$SnSe_2$ heterostructure for high performance photodetector. *Adv. Opt. Mater.* **2024**, *12*, 2303088.
[27] Lu, J. T.; Zheng, Z. Q.; Yao, J. D.; Gao, W.; Zhao, Y.; Xiao, Y.; Li, J. B. 2D In_2S_3 nanoflake coupled with graphene toward high-sensitivity and fast-response bulk-silicon schottky photodetector. *Small* **2019**, *15*, 1904912.
[28] Liu, Y. C.; Zhang, Y. X.; Zhao, K.; Yang, Z.; Feng, J. S.; Zhang, X.; Wang, K.; Meng, L. N.; Ye, H. C.; Liu, M. et al. A 1300 mm^2 ultrahigh-performance digital imaging assembly using high-quality perovskite single crystals. *Adv. Mater.* **2018**, *30*, 1707314.
[29] Ismail, R. A.; Khashan, K. S.; Mahdi, R. O. Characterization of high photosensitivity nanostructured 4H-SiC/p-Si heterostructure prepared by laser ablation of silicon in ethanol. *Mater. Sci. Semicond. Process* **2017**, *68*, 252–261.
[30] Jehad, A. K.; Unverdi, O.; Celebi, C. High voltage response of graphene/4H-SiC UV photodetector with low level detection. *J. Alloys Compd.* **2023**, *969*, 172288.
[31] Zhang, R. J.; Liu, J.; Liu, G.; Yao, L.; Liu, Y.; Hong, R. D.; Zhang, F. A dual P-layer 4H-SiC P-I-N photodetector for the detection from extreme ultraviolet to ultraviolet-A. *Electron. Lett.* **2023**, *59*, e12953.
[32] Yu, J. G.; Nie, Z. Z.; Dong, L. P.; Yuan, L.; Li, D. J.; Huang, Y.; Zhang, L. C.; Zhang, Y. M.; Jia, R. X. Influence of annealing temperature on structure and photoelectrical performance of β-Ga_2O_3/4H-SiC heterojunction photodetectors. *J. Alloys Compd.* **2019**, *798*, 458–466.
[33] Sun, C. Z.; Chen, X. F.; Hong, R. D.; Li, X. M.; Xu, X. G.; Chen, X. P.; Cai, J. F.; Zhang, X. A.; Cai, W. W.; Wu, Z. Y. et al. Enhancing the photoelectrical performance of graphene/4H-SiC/graphene detector by tuning a Schottky barrier by bias. *Appl. Phys. Lett.* **2020**, *117*, 071102.
[34] Wang, K. T.; Wang, H. L.; Chen, C. M.; Li, W. J.; Wang, L.; Hu, F.; Gao, F. M.; Yang, W. Y.; Wang, Z. X.; Chen, S. L. High-performance ultraviolet photodetector based on single-crystal integrated self-supporting 4H-SiC nanohole arrays. *ACS Appl. Mater. Interfaces* **2023**, *15*, 23457–23469.
[35] Kyoung, S.; Jung, E. S.; Sung, M. Y. Post-annealing processes to improve inhomogeneity of Schottky barrier height in Ti/Al 4H-SiC Schottky barrier diode. *Microelectron. Eng.* **2016**, *154*, 69–73.
[36] Shigiltchoff, O.; Bai, S.; Devaty, R. P.; Choyke, W. J.; Kimoto, T.; Hobgood, H. M.; Neudeck, P. G.; Porter, L. M. Schottky barriers for Pt, Mo and Ti on 6H and 4H SiC (0001), $(000\bar{1})$, $(1\bar{1}00)$ and $(1\bar{2}10)$ faces measured by *I–V*, *C–V* and internal photoemission. *Mater. Sci. Forum* **2003**, *433–436*, 705–708.
[37] Yu, Y. L.; Shen, T.; Long, H. R.; Zhong, M. Z.; Xin, K. Y.; Zhou, Z. Q.; Wang, X. Y.; Liu, Y. Y.; Wakabayashi, H.; Liu, L. Y. et al. Doping engineering in the MoS_2/$SnSe_2$ heterostructure toward high-rejection-ratio solar-blind UV photodetection. *Adv. Mater.* **2022**, *34*, 2206486.
[38] Zheng, Z. Q.; Chen, P. F.; Lu, J. T.; Yao, J. D.; Zhao, Y.; Zhang, M. L.; Hao, M. M.; Li, J. B. Self-assembly In_2Se_3/$SnSe_2$ heterostructure array with suppressed dark current and enhanced photosensitivity for weak signal. *Sci. China Mater.* **2020**, *63*, 1560–1569.
[39] Renz, A. B.; Shah, V. A.; Vavasour, O. J.; Baker, G. W. C.; Bonyadi, Y.; Sharma, Y.; Pathirana, V.; Trajkovic, T.; Mawby, P.; Antoniou, M. et al. The optimization of 3.3 kV 4H-SiC JBS diodes. *IEEE Trans. Electron Devices* **2022**, *69*, 298–303.
[40] Radhakrishnan, R.; Zhao, J. H. A 2-dimensional fully analytical model for design of high voltage junction barrier Schottky (JBS) diodes. *Solid-State Electron.* **2011**, *63*, 167–176.